Title

A wearable patch for continuous levodopa monitoring in sweat: Towards exertion and power-free pharmacodynamic assessment in Parkinson's disease

Journal

Proceedings of the National Academy of Sciences of the United States of America, 123(32)

ISSN

0027-8424

Authors

Saha, Tamoghna

Khan, Muhammad Inam

Longardner, Katherine

et al.

Publication Date

2026-08-11

DOI

10.1073/pnas.2610453123

PNAS RESEARCH ARTICLE | ENGINEERING MEDICAL SCIENCES

A wearable patch for continuous levodopa monitoring in sweat: Towards exertion and power-free pharmacodynamic assessment in Parkinson's disease

Tamoghna Saha[a,1], Muhammad Inam Khan[a,1], Katherine Longardner[b,1], Barak Sabbagh[a], Kaiwen Zheng[c], Hugo de Mendoza[d], Gaoyuan Ji[c], Bumsik Choi[a], Zongnan Wang[d], Rosie Pham[a], Michael Skipworth[b], Eshita Shah[c], Maria Reynoso[a], Chochanon Moonla[a], Abdulhameed Abdal[d], Debika Datta[a], Samar Singh Sandhu[a], Ponnusamy Nandhakumar[a], Artur Jedrzak[a], Shichao Ding[a], Lu Yin[a], Irene Litvan[b,2], and Joseph Wang[a,2]

Affiliations are included on p. 10.

Edited by Xue Feng, Tsinghua University, Beijing, China; received March 24, 2026; accepted June 26, 2026 by Editorial Board Member Yonggang Huang

Precision management of Parkinson's disease (PD) requires frequent levodopa (L-dopa) dose adjustments, yet current monitoring relies on subjective symptom reporting and infrequent blood testing. Here, we present a soft, fingertip-mounted wearable platform for continuous, noninvasive L-dopa monitoring. By combining osmotically harvested passive sweat with soft hydrogels, a potentiometric sensing strategy, and individualized calibration, the platform estimates blood L-dopa information from sweat without external power or iontophoresis. Strong correlations between sweat and high-performance liquid chromatography (HPLC)-measured blood L-dopa concentrations were observed in healthy ($Pr = 0.85$) and PD subjects ($Pr = 0.88$) following a single immediate-release L-dopa/carbidopa dose. Low motor symptom scores aligned with peak L-dopa levels, confirming pharmacodynamic relevance. L-dopa cleared faster in PD patients despite similar bioavailability to healthy subjects, while recorded hemodynamic responses showed short hypotensive trends for both groups. Machine learning identified sweat and blood pressure as key contributors toward accurate estimation of blood L-dopa levels (mean absolute error = 2.02 μM vs. ground truth). Overall, our easy-to-use, energy-efficient wearable supports real-time, stimulation-free monitoring, potentially enabling at-home dosage adjustments and paving the way for future autonomous closed-loop L-dopa therapeutic system development.

levodopa monitoring | Parkinson's disease | clinical trials | continuous sweat sensing | wearable devices

Significance

Effective management of Parkinson's disease (PD) requires dynamic adjustment of levodopa dosing. Current approaches rely on subjective symptom reporting and infrequent blood sampling. We introduce here a soft, fingertip-mounted wearable enabling continuous, noninvasive levodopa monitoring at rest using passively extracted sweat, eliminating the need for exercise or iontophoretic stimulation. By integrating a potentiometric sensing strategy with individualized calibration, the platform accurately estimates blood levodopa levels from sweat with no power consumption, showing strong agreement with gold-standard measurements in both healthy and patient populations. The device captures pharmacodynamic responses and patient-specific clearance trends, while machine learning enhances prediction accuracy. This approach establishes a foundation for real-time, at-home therapeutic optimization and advances the development of future closed-loop treatment systems for PD.

Parkinson's disease (PD) is the second most common and fastest-growing neurodegenerative disorder worldwide (1, 2). The projected number of people living with PD in the United States is expected to reach ~2 million by 2040, with a total expenditure ranging ~$80 billion (3). Aggregation of misfolded alpha-synuclein protein in PD is associated with progressive deterioration of the nigrostriatal pathway—a brain network for motor control, resulting in depletion of the neurotransmitter dopamine, which leads to numerous symptoms (4, 5). Motor symptoms i.e., manifestations of PD affecting movement include bradykinesia (slowness), tremor (shaking), and muscular rigidity (stiffness), while nonmotor symptoms can include olfactory, autonomic, sleep, and neuropsychiatric impairments (6, 7). While no cure for PD exists, levodopa (L-dopa) is the most effective symptomatic treatment, which is typically administered via oral tablets or capsules, and in advanced cases, through inhaled powder or continuous intrajejunal or subcutaneous infusions (8–10).

L-dopa crosses the blood–brain barrier and is converted to dopamine in the brain (Fig. 1*A*) to temporarily ameliorate symptoms of dopamine deficiency. To promote greater bioavailability in the brain and prevent adverse effects (e.g., nausea, hypotension) in clinical practice, L-dopa is administered with an aromatic amino acid dopa-decarboxylase inhibitor such as carbidopa, usually in 4:1 or 10:1 ratio (11). The typical therapeutic L-dopa concentration in plasma and cerebrospinal fluid ranges from ~2 to 10 μM and ~0.5 to 1.5 μM, respectively (12). Despite being the "gold standard" for treating PD motor symptoms since the 1960s, L-dopa therapy presents numerous challenges. L-dopa has a short elimination half-life (~0.5 to 1.5 h) and is rapidly metabolized in the gut and tissues by aromatic amino acid decarboxylase and catechol-o-methyl transferase enzymes, reducing its bioavailability. Numerous gastrointestinal factors such as food intake, slowed motility, and gut microbiome composition can impair L-dopa's absorption and transport (13). Furthermore, while most PD patients initially experience uncomplicated symptomatic

This article is a PNAS Direct Submission. X.F. is a guest editor invited by the Editorial Board.

[1]T.S., M.I.K., and K.L. contributed equally to this work.

[2]To whom correspondence may be addressed. Email: ilitvan@health.ucsd.edu or josephwang@ucsd.edu.

This article contains supporting information online at https://www.pnas.org/lookup/suppl/doi:10.1073/pnas.2610453123/-/DCSupplemental.

Published July 27, 2026.

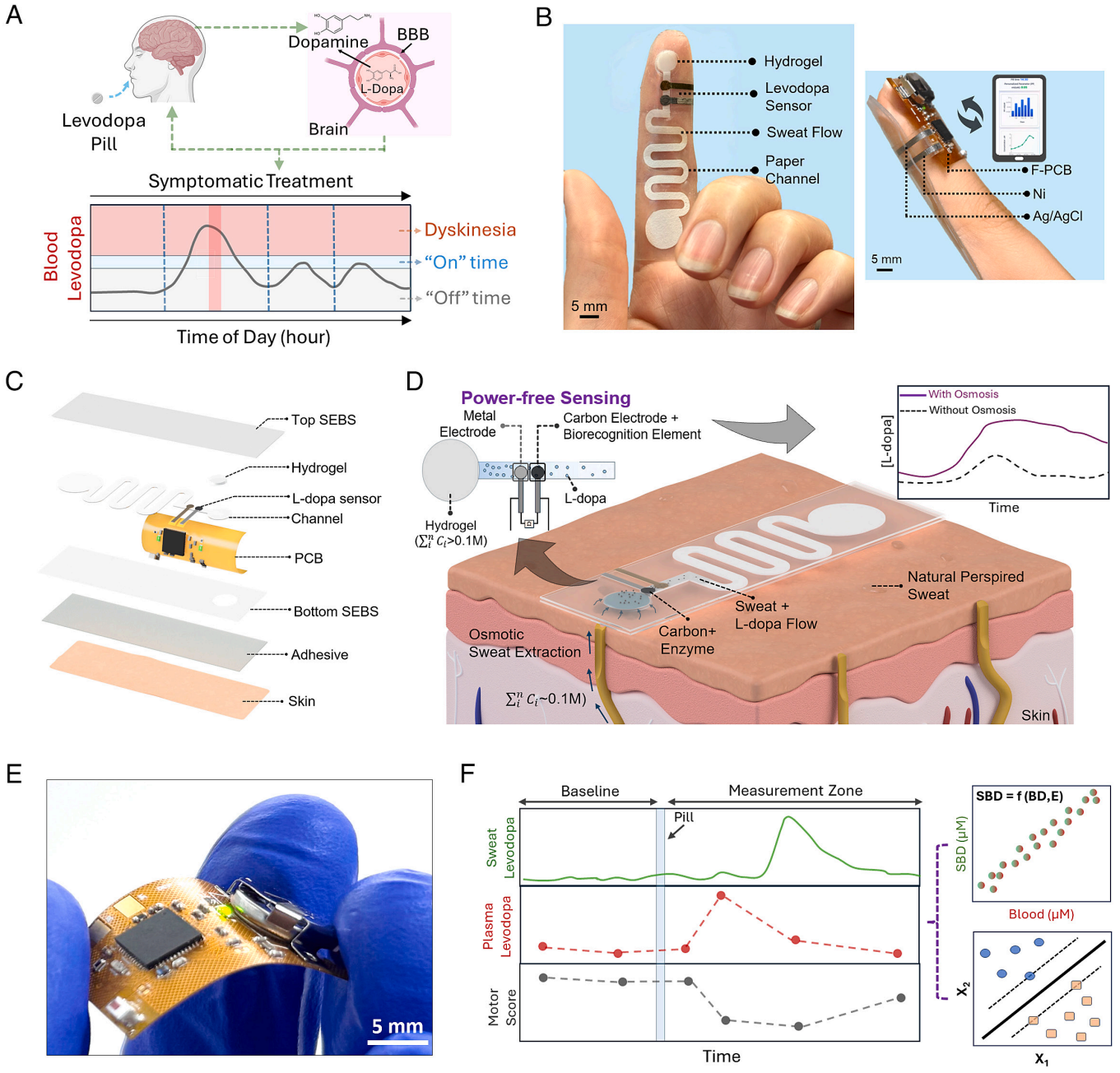

Fig. 1. Schematic highlighting the motivation, approach, and deliverables of S-CDM. (*A*) PD causes various motor symptoms, which occur due to depletion of dopamine in the nigrostriatal pathways. Orally administered L-dopa can improve PD motor symptoms, since it crosses the blood–brain barrier (BBB) and is converted to dopamine in the brain to temporarily restore L-dopa levels. The goal is to maintain the optimal (blue shaded zone) therapeutic levels all times. Orange: Low risk, Blue: High risk. (*B*) The integrated osmotic sweat patch fits conformally on the skin, which comprises (*C*) a hydrogel, paper fluidic channel, two-electrode sensing system, flexible printed circuit board, and covers. (*D*) The hydrogel withdraws sweat passively and continuously from the skin at rest, while the power-free biosensor functions on potentiometric mechanism. C_i: Concentration of each solute. (*E*) Optical image of the FPCB (*F*) Sweat, vital signs, and plasma L-dopa levels are measured in conjunction with motor score under clinical settings. Personalized equations can be established for each subject to estimate L-dopa concentration dynamics from sweat readings. All these parameters are fused to train a ML model and derive blood L-dopa levels.

relief from L-dopa, over time, most develop motor complications in response to it. These motor symptom fluctuations include premature or unpredictable decreases of L-dopa's beneficial effect ("off time") when L-dopa levels are subtherapeutic, resulting in worsening parkinsonian symptoms (e.g., slowness, stiffness, tremor); conversely, when levels are therapeutic or supratherapeutic, individuals may experience excessive involuntary movements (dyskinesias) (14). Thus, L-dopa therapy in PD is highly personalized and depends on each individual's daily schedule, activities, and symptoms. At present, clinicians adjust L-dopa therapy based on patients' self-reported symptoms and a brief clinical observation. However, these approaches fail to accurately capture an individual's medication response and functional status, particularly in PD patients with symptom fluctuations, underscoring the urgent need for improved methods to monitor and adjust L-dopa dosing throughout the day to prevent disabling symptoms.

Historically, plasma has been the primary biofluid for L-dopa quantification, which is analyzed through techniques such as liquid chromatography–mass spectroscopy (LC–MS). However, this method has many drawbacksvit is costly, needs to be conducted in centralized laboratories, requires venipuncture and trained personnel, and has long turnaround times (typically ~ weeks). Therefore, the

current methods for L-dopa concentration measurements cannot be used to guide real-time medication dosage adjustments. Hence, alternative biofluids (like interstitial fluid and sweat) and techniques have been explored to measure L-dopa in the ambulatory setting in near-real time with rapid turnaround using minimally invasive techniques (15). Our group has previously developed point-of-care platforms for quantifying L-dopa in capillary blood and sweat (14, 16). However, these platforms also have limitations; they rely on frequent measurements, generate only episodic L-dopa concentration profiles, demand constant user attention, consume power (via amperometric or voltammetric techniques), and are highly vulnerable to external contamination. Since PD predominantly involves high motor dysfunctionality, continuous and accurate monitoring platforms for L-dopa with minimal user intervention (like attach and forget) is an essential requirement (17). Furthermore, continuous L-dopa monitoring devices could eventually be combined with existing continuous infusion technologies in a closed-loop system to provide automated, individualized PD management. Hence, operating with power efficient components is necessary to support extended operation for such devices. Looking ahead, efficient hardware alone is insufficient as intelligent data interpretation is also needed to translate continuous sensing signals into clinically actionable insights. Hence, the use of machine learning (ML) models in PD analysis can enable predictive insights and help identify the key factors that predominantly influence outcomes.

To address these limitations of L-dopa concentration measurements, we have developed an integrated wearable sweat-based continuous L-dopa monitoring (S-CDM) patch that functions at the fingertip with no physical exertion or power consumption required (Fig. 1*B* and *SI Appendix*, *Supporting Information Text 1*). The fingertip is targeted due to its high sweat gland density (~400 glands/cm^2) possession (18). The patch conformally sits at the fingertip with all sensing components encapsulated within two styrene ethylene butylene styrene (SEBS) sheets (Fig. 1*C*). The L-dopa sensor interfaces the paper fluidic channel near the hydrogel site (inlet) and is connected to the flexible printed circuit board (FPCB) for wireless data transmission (visible from the dorsal side of the fingertip). The hydrogel rests over the circular part of the paper channel, which interfaces with the skin for sweat collection. The extended serpentine channel design maintains capillary pressure and promotes unidirectional forward flow, thereby preventing mixing between old and new sweat. The patch dimensions range 70 mm × 25 mm, and it runs on passive sweat and potentiometric sensing. Passive sweat harvesting is conducted using a hydrogel that possesses a higher osmotic strength vs. sweat inside the skin, while a two-electrode system running on open circuit potential (OCP) enables power-free L-dopa biosensing (Fig. 1*D*). The hydrogel's osmotic strength is elevated through equilibration in a highly concentrated benign solution. Osmotic sampling leads to greater L-dopa flow in the channel with minimal sweat rate fluctuations (19). At the fingertip flow rate (~75 to 300 nL/min), the channel accommodates ~48 µL of fluid and saturates within ~6 to 7 h (*SI Appendix*, Fig. S1). This duration is sufficient to capture pharmacodynamics and pharmacokinetics (PK) of L-dopa from at least two doses of immediate-release oral L-dopa. The potentiometric sensor comprises a metal electrode (anode) and a carbon electrode coated with tyrosinase enzyme (cathode), connected via an external load. A metal electrode allows faster cell discharge during baseline stabilization (*SI Appendix*, Fig. S2). The FPCB (18 mm × 27 mm) was designed around nRF52832 and is powered by a coin cell battery (Fig. 1*E*).

In our pilot study, we evaluated the feasibility of creating individualized L-dopa profiles and examined the relationship between L-dopa concentrations in sweat and plasma to determine the potential of using sweat as an alternative biofluid (to blood) for continuous L-dopa monitoring. We first aimed to assess the relationship between fingertip sweat and capillary blood L-dopa concentrations in healthy volunteers following fava bean ingestion, and in both healthy controls and individuals with PD after administration of immediate-release oral L-dopa/carbidopa pill. We examined associations between sweat-blood plasma L-dopa levels, vital signs (20, 21), and PD motor symptom severity (22, 23) following medication intake. (Fig. 1*F*). Finally, we used ML to fuse all measured parameters to predict blood plasma L-dopa levels and validated it against HPLC-measured plasma L-dopa concentration.

Results

Osmotic Hydrogel Performance for Passive Sweat Extraction. The hydrogel comprises a semi-interpenetrating polymer network of polyvinyl alcohol (PVA) and polyacrylamide (PAAm), equilibrated with 20 wt.% ethylene glycol (EG_{20}) solution for lowering the chemical potential of water (osmotic strength elevation), relative to that of sweat underneath the skin (Fig. 2*A*). The phenomenon can be defined by

$$\pi = \frac{\mu_w^{gel} - \mu_w^{sweat}}{V_w},$$

where, π: osmotic pressure, μ_w^{sweat}: chemical potential of water (w) in sweat, μ_w^{gel}: chemical potential of water in the hydrogel, and V_w: partial molar volume of water. Such a low concentrated solution maintains the sensor's optimal performance, as L-dopa levels in sweat are naturally low vs. common metabolites (~20× than glucose and ~1,000× than lactate) (*SI Appendix*, Fig. S3) (4, 19, 24, 25). The hydrogel is soft, bendable, and benign to the skin upon contact (Fig. 2*A*). The FTIR peaks confirmed the functional groups after EG_{20} treatment (Fig. 2*B*). A blend of sharp and skewed peaks around 3,200 to 3,700 cm^{-1} indicates O–H and N–H presence. Higher intensity in PVA-PAAm-EG is due to O–H in EG. The sharp peak around 1,600 to 1,800 cm^{-1} in PAAm, PVA-PAAm, and PVA-PAAm-EG is from C=O in acrylamide. The peak around 1,000 to 1,200 cm^{-1} in PVA-PAAm-EG can be attributed to the increasing C–O stretching from EG. We investigated two solvents to treat our hydrogels for optimal sweat collection–deionized (DI) water and phosphate buffer saline (1× PBS). Both hydrogels could compress up to ~70% of their thickness, and the relatively higher stiffness with EG_{20} and PBS treatment (vs. EG_{20} + DI water equilibration) can be attributed to cumulative effects from hydrogen bonding between EG and polymer chains, and from ionic crosslinking due to PBS (Fig. 2*C* and *SI Appendix*, Fig. S4). Storage modulus (G') of EG_{20}/PBS being higher and lower than EG_{20}/DI and 1× PBS, respectively, at intermediate strain rates (0.1 to 1 s^{-1}) justifies that EG relaxes ionic crosslinking density and consequently promotes greater sweat uptake upon skin contact. Both hydrogels were mechanically resilient and could bear 15 cycles of loading and unloading without showing any hysteresis, confirming their reusable capabilities (Fig. 2*D*). To determine the sweat withdrawing capacity, theoretical swelling pressure (π_{tot}) was calculated for both hydrogels using the Flory–Rehner theory:

$$\pi_{tot} = -V_1^{-1}\left(\frac{\partial \Delta F_{tot}}{\partial n_1}\right) = \pi_{el} + \pi_{mix} + \pi_{ion},$$

where V_1 is the solvent molar volume, ΔF_{tot} is the net change in total free energy, n_1 is the number of moles of solvent, π_{tot} is the total gel swelling pressure and π_{el}, π_{mix}, and π_{ion} are the elastic, mixing, and

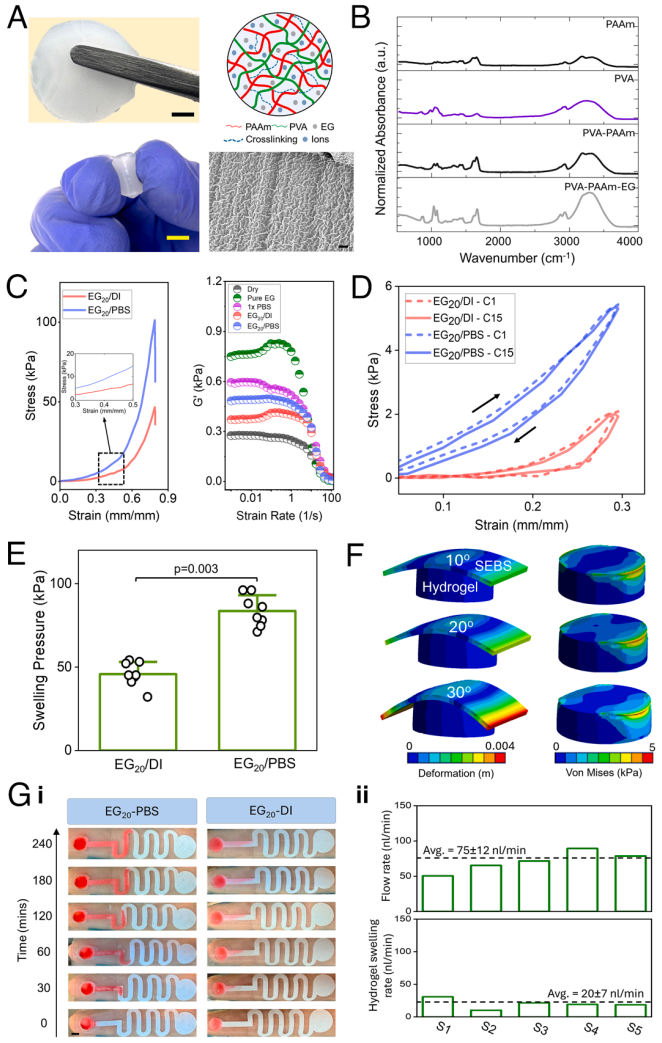

Fig. 2. Mechanical characterization of hydrogel with on-body performance. (*A*) Optical and scanning electron microscopy image of the PVA-PAAm-EG_{20} hydrogel. (*B*) FTIR absorbance spectra of different hydrogel variants. (*C*) Plot showing the compression strength and rheological properties of the hydrogel variants. (*D*) Hysteresis plot of the hydrogel variants after 15 cycles of loading and unloading. C1—1st cycle, C15—15th cycle. (*E*) Plot with estimated swelling pressure values of the hydrogels. n = 8, P = 0.003 from the unpaired two sample t test. All studies were conducted using Mark 10 Force and Torque Measurement System. (*F*) Stress and deformation profiles experienced by the PVA-PAAm-EG hydrogel top surface from 10^0 to 30^0 bending of top SEBS layer after on-finger mount. (*Gi*) Optical images showing dye progression in patch from the two hydrogel variants in a single subject. (Scale bar, 2 mm.) (*Gii*) This test was conducted on five healthy subjects from which sweat rate and hydrogel swelling rate are estimated.

ionic contributions to the total swelling pressure, respectively. π_{tot} of EG_{20}/PBS hydrogel was greater than EG_{20}/DI, suggesting its greater sweat withdrawing capacity upon skin contact (Fig. 2*E* and *SI Appendix, Supporting Information Text 2*). Moreover, since the hydrogel experiences stress from the bending of SEBS layers during on-finger experiments (Fig. 2*F*), we conducted finite element analysis (FEA) simulations to estimate this stress distribution across the top hydrogel surface (*SI Appendix*, Fig. S5 and *Supporting Information Text 3*). Assuming a 30° bending angle (of SEBS layer vs. skin plane), we observe stresses to be majorly confined at the hydrogel edges and its maximum magnitude ~5 tro 7% of π_{tot} (Movie S1). Thus, swelling-induced mechanical pressure exerted by the hydrogel exceeds the pressure applied by SEBS. These values confirm that the EG_{20}/PBS hydrogel holds enough capacity to uptake sweat without leaching (from excessive mechanical pressure) any solution onto the paper channel (i.e., causing no analyte dilution) upon skin contact.

The EG_{20}/PBS hydrogel led to greater dye flow on-finger, with sweat rate and hydrogel swelling rate ranging ~75 ± 12 nL/min and ~20 ± 7 nL/min, respectively, during a 5-h study with five subjects (Fig. 2 *G, i* and *ii* and *SI Appendix*, Fig. S6). This is mostly due to the synergistic interaction between the ions and the osmolyte, which together promotes enhanced dye accumulation. Results also highlight the limited hydrogel's capacity to absorb sweat and eventually allowing most of it to pass into the channel. We believe that these flow rates are unlikely to be significantly affected by changes in ambient temperature or humidity, as osmosis is a colligative property in which fluid transport depends primarily on the chemical potential difference of water between the hydrogel and the skin.

Power-Free L-dopa Biosensor Performance. L-dopa electrochemical sensing has traditionally followed two routes: a) nonenzymatic direct oxidation and b) enzymatic reduction (14, 16, 26–28). Both techniques require an external potentiostat to initiate the electrochemical detection reaction and consume power (ranging from μW to mW). Additionally, the direct oxidation pathway (~0.2 to 0.4 V) can even make the sensor response vulnerable to interference from common electroactive species (like ascorbic acid and uric acid) in sweat (29). Hence, to make these sensors independent of such factors and compatible for energy efficient bioelectronic integration, a potentiometric enzymatic redox cycling mechanism is presented here. The L-dopa sensor comprises a sputtered Ni anode and a screen printed tyrosinase-modified carbon cathode (Fig. 3*A* and *SI Appendix*, Fig. S7). Ni oxidation in the presence of buffer generates an electron flow in the external circuit, which reduces dopaquinone (DQ) to sustain the redox reaction. Both electrodes are connected by an external load. The reaction mechanism follows as

$$\mathrm{Ni} - 2e^- \rightarrow \mathrm{Ni}^{+2}\ E^o = 0.25\ \mathrm{V\ vs.\ Ag/AgCl},$$

$$\mathrm{L-dopa} + \mathrm{O_2} \rightarrow \mathrm{DQ} + 2e^- + \mathrm{H_2O}\ E^o = -0.02\ \mathrm{V\ vs.\ Ag/AgCl}.$$

Based on the above two reactions, the total OCP window ranges ~−0.27 V, which is proximal to DQ's reduction potential (−0.3 V for chronoamperometry) (*SI Appendix*, Fig. S7) (14). We first investigated oxidation pathway of Ni through cyclic voltammetry (CV) in different biological buffers (pH 5.5 to 7.5) and in PBS solution of varying pH (Fig. 3*B*). Results revealed that phosphate ions from the PBS buffer (vs. OH^- or COO^- in HEPES and MES) and lower solution pH majorly contribute toward favoring Ni oxidation at −0.3 V. Moreover, the long-term minimal effect of Ni passivation and Ni^{+2} release on the full cell response under varying ionic strength is shown in *SI Appendix*, Fig. S8. The external load resulting in the highest signal resolution was derived through linear sweep voltammetry (LSV) (Fig. 3*C*). Unlike a typical LSV plot, here we determined the optimal load from E vs. E/I plot, generated after discharging the full cell from OCP to 0 V (30, 31). LSV shows that 10^6 to 10^7 Ω leads to highest signal resolution at the physiological concentration (1 to 30 μM). This is also verified through in-vitro calibration studies (*SI Appendix*, Fig. S9). However, a high external load decreases the discharge current flow during baseline stabilization. This may not be desirable for patients in the ambulatory setting, as the subject would have to wait long for the cell to be fully discharged before taking the pill in order to see distinct L-dopa signals. Thus, 1M Ω was chosen as the acceptable external load. The linear dynamic range of the sensor ranged up to 35 μM, with a sensitivity and limit of detection (LOD) of ~1 mV/μM and ~0.13 μM, respectively

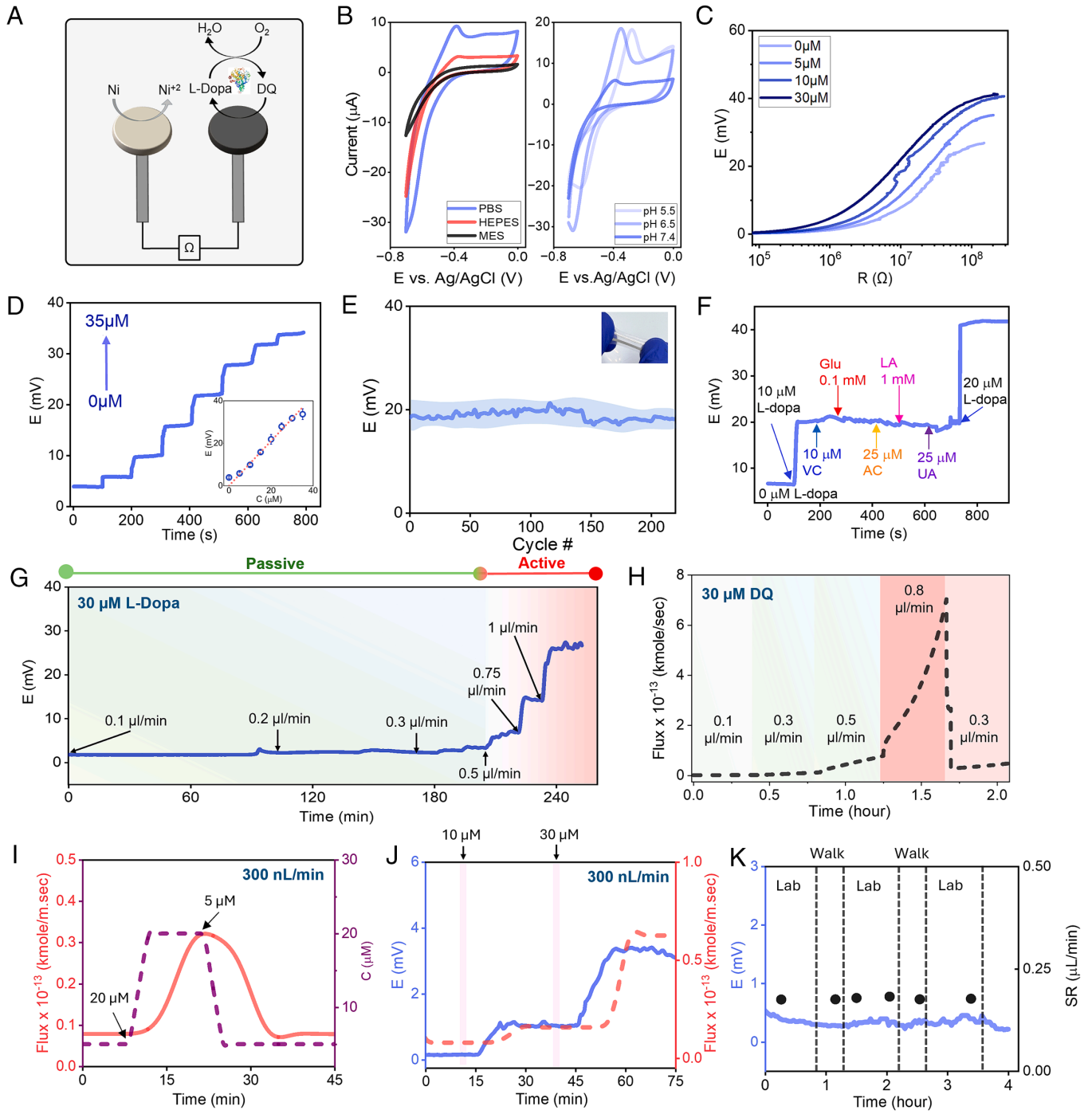

Fig. 3. Analytical performance of L-dopa biosensor. (*A*) Schematic highlighting the self-powered redox cycling mechanism of the L-dopa detection for a Ni-carbon-tyrosinase electrode system. *Inset*: Tyrosinase enzyme. (*B*) Cyclic voltametric plots comparing Ni oxidation limits in different biological buffers and in 1× PBS solution of varying pH. HEPES: (4-(2-hydroxyethyl)-1-piperazineethanesulfonic acid), MES: 2-(N-morpholino) ethanesulfonic acid. (*C*) LSV plot to estimate the external resistance for detection. The X-axis denotes (E/I). Scan rate: 1 mV/s. (*D*) Potentiometric plot with calibration (*Inset*). Error bars denote SD from N = 3 sensors. (*E*) Stability of 20 μM L-dopa response vs. Ag/AgCl reference till 200 cycles of 20% strain. Blue shaded zone: 95% CI from N = 3 sensors. *Inset*: Images of electrodes under stretching. (*F*) Interference study with common sweat analytes. VC: Vitamin C, Glu: Glucose, AA: Ascorbic acid, UA: Uric acid, Ac: Acetaminophen, LA: Lactic acid. (*G*) Effect of flow rate on the sensor response for 30 μM L-dopa. (*H*) FEA simulations showing flux from 30 μM dopaquinone (DQ) over time under varying flow rates. (*I*) FEA simulations showing flux trends over time under dynamic increase and decrease of L-dopa inlet concentration at a constant flow rate. (*J*) Comparison of FEA simulations vs. experimental data for increments of 10 μM and 30 μM L-dopa at constant flow rate. (*K*) Plot showing the signal stability under varying physiological activities. SR: Sweat rate.

(Fig. 3*D* and *SI Appendix*, Fig. S10). The sensors can even retain their electrochemical performance up to 200 cycles of repetitive physiological stretching (~30% of their original length, Fig. 3*E* and *SI Appendix*, Fig. S11). It is unresponsive without the enzyme and independent of the interference from other common sweat analytes in PBS (Fig. 3*F* and *SI Appendix*, Fig. S12). Since the electrolyte concentrations in PBS are comparable to those in sweat, we expect the sensor response to remain largely unaffected by electrolyte variations. Comedication Carbidopa also did not show any interference (*SI Appendix*, Fig. S13). The net potential change between pH 5.5 and 6.5 is insignificant ($P = 0.012$) under 30 μM (*SI Appendix*, Fig. S14). This validates that typical sweat pH (pH

5.5 to 6.5) will not affect the sensor reading nor require pH-based corrections (29). However, the signal change decreases by ~35% at pH 7.5 (P = 0.004 vs. pH = 5.5), signifying increased chances of error at higher pH measurements. This is also a result of the low Ni oxidation rate at pH 7.5 and −0.3 V, which in turn supplies fewer electrons for L-dopa reduction at the cathode (Fig. 3*B*). Temperature and humidity variations had no significant effect on the sensor response (*SI Appendix*, Figs. S15 and S16). The same sensor could withstand up to 10 cycles of repetitive spiking (of 10 μM) with a net drift of ~0.1 mV/cycle, while intersensor relative SD ranged ~9.1%. The sensor also demonstrated good reversibility behavior in-vitro and under flow conditions (*SI Appendix*, Fig. S17). Next, the effect of sweat rate was investigated. The potential readings were lower (vs. Fig. 3 *D* and *F*) in the flow system due to higher solution resistance arising from the reduced fluid volume present between the channel and sensor. The potential change stays independent of sweat rate till 0.5 μL/min flow for 30 μM, arising due to low DQ production from limited influx of L-dopa (Fig. 3*G*). Beyond 0.5 μL/min, the net potential change followed ~45 mV/(μL min) due to convection effects and high DQ production (*SI Appendix*, Fig. S18). Hence, under active sweat regime (>0.5 μL/min), the sensor reading is more sensitive to flow rate changes, so the response would require adjustment with a correction factor (based on measured sweat rate by a sweat rate sensor) for accurate concentration estimation. Plain buffer solution flow at these varying flow rates did not show any response, proving the response to be solely coming from L-dopa (*SI Appendix*, Fig. S19). FEA flow simulations also showed similar effects, where the net dopaquinone flux could vary up to ~1 to 20^{-13} (kmol/s)/(μL/min) under active sweat rate regime (Fig. 3*H* and *SI Appendix*, Fig. S20). The flux drastically changes when transitioning from active to passive regime (as shown from 0.8 to 0.3 μL/min in Fig. 3*H*), proving that sweat L-dopa levels are more accurate when measured under passive sweat rates (Movie S2 and *SI Appendix, Supporting Information Text 4*). FEA simulations were also conducted at the fingertip flow rate (~0.3 μL/min) for varying L-dopa concentrations (*SI Appendix*, *Supporting Information Text 5* and Figs. S21–S23) (19). Fig. 3*I* shows that upon spiking and dropping the inlet concentration (purple dotted line), the onset of sensor response (orange line) lags by ~5 to 7 min (pink shaded region). This is an outcome from the sensor being located ~1.3 cm away from the inlet, and this adjustment has been accounted in all on-body trials. FEA simulation results were also compared with experimental results (blue line) at 0.3 μL/min in Fig. 3*J* (*SI Appendix*, Tables S1 and S2). The trends are in match with both 10 and 30 μM L-dopa increase, with a ~5 min onset lag time. Finally, the S-CDM was tested under mild daily activities with an impedimetric based sweat rate sensor (Fig. 3*K* and *SI Appendix*, Fig. S24) (19). Insignificant signal drifts were observed during walking and lab work, reflecting the minimal sweat rate influence under osmotic sampling. Such stable trends were even observed under simulated PD tremor (4 to 8 Hz) and finger snapping (Movie S3). A comparative analysis with touch-based L-dopa sensing devices, highlighting the advantages of our S-CDM platform, is presented in *SI Appendix*, Table S3.

S-CDM Performance in Healthy Subjects. The S-CDM was first validated after fava bean (FB) consumption in five healthy subjects, as fava beans contain L-dopa (~50 to 100 mg L-dopa per 100 gm beans) (28, 32, 33). The net sensor potential change ($\Delta E(t)$) ranged ~8 to 10 mV across all subjects, and multiple fava bean dosages were also detectable (*SI Appendix*, Fig. S25). The sensor data were validated against fingertip capillary blood using our previously developed assay, where the net capillary blood L-Dopa concentration change (ΔBD) ranged from ~6 to 10 μM, with a Pearson's correlation coefficient (Pr vs. ΔE) of 0.70, indicating a reasonable correlation (*SI Appendix*, Fig. S25) (16). To acquire further insights from these data, we developed a two-point calibration model (between ΔE vs. ΔBD) to estimate the sweat derived blood L-dopa concentration ($SBD(t)$) over time and evaluate its correlation to the measured blood L-dopa ($BD(t)$) concentration (Fig. 4*A* and *SI Appendix*, *Supporting Information Text 6*). Such a model would: a) effectively capture and assist analyzing parameters that affect L-dopa pharmacokinetics, b) help users comprehend how these parameters vary during daily activities, and c) facilitate blood calibration-free estimation of L-dopa concentration (34). The model assumes: a) No L-dopa is initially present in the blood before pill intake. b) Highest change in sensor response occurs only from and after maximum $BD(t)$. Based on this, $SBD(t)$ equation is

$$SBD(t) = \left(\frac{E(t) - E_0}{\Delta E_{max}}\right)\Delta BD_{max}, \qquad [1]$$

where, $SBD(t)$: sweat derived blood L-dopa concentration, ΔE_{max}: maximum change in L-dopa potential, ΔBD_{max}: maximum change in blood L-dopa concentration, and E_0: baseline potential. Capillary blood L-dopa concentration was estimated with our previously developed assay and the derived personalized coefficients $\left(\frac{\Delta E_{max}}{\Delta BD_{max}}\right)$ values from the model ranged ~ 1.02 ± 0.14 mV/μM (Fig. 4*B* and *SI Appendix*, Figs. S26 and S27) (14). The inter- and intrasubject coefficient values exhibited negligible variation across multiple tests over time, indicating that this fixed value can serve as a personalized signature for $BD(t)$ estimation from sweat in real time, eventually eliminating the need for frequent blood calibrations. This calibration-free approach has been demonstrated for sweat glucose, and observing a similar trend for L-dopa suggests it could be applied here as well (19, 35). This personalized approach improved the Pr (to 0.85) and resulted in average blood's area under the curve for 90 min ($AUC_{0-90,BD}$) to range ~ 234 ± 51 μM. min (*SI Appendix*, Fig. S28). The L-dopa clearance followed first-order kinetics with a clearance rate (k) of ~0.03 ± 0.01 μM/min and apparent elimination half-life in blood ($t_{1/2,BD}$) of ~23 ± 8.10 min.

The S-CDM was next evaluated in three healthy individuals after taking a single oral tablet of immediate-release L-dopa/carbidopa, 100 mg/25 mg (*SI Appendix*, Table S4). The potentiometric response and HPLC calibration are shown in *SI Appendix*, Figs. S29 and S30. $\Delta E(t)$ ranged ~0.6 mV, 0.03 mV, and 0.03 mV in subject 1, 2, and 3, respectively, while average $\frac{\Delta E_{max}}{\Delta BD_{max}}$ (from Eq. **1**) ranged ~ 0.04 mV/μM (Fig. 4*B*). Fig. 4 *C, i–iii* shows the $BD(t)$ and $SBD(t)$ trends from three subjects. L-dopa clearance in blood for subject 1 followed first-order kinetics. The k and $t_{1/2,BD}$ ranged ~0.015 μM/min and ~44 min, respectively, in subject 1 (*SI Appendix*, Fig. S31). Maximum blood plasma L-dopa concentration ($C_{max,BD}$) and time to peak ($t_{max,BD}$) were ~5.8 μM and ~30 min, respectively (Fig. 4 *C, i*). These timelines are consistent with previous clinical reports, reflecting the typical duration required for L-dopa absorption in the gut (36, 37). The time lag ($t_{lag,SBD}$) vs. $BD(t)$ peak, $AUC_{0-90,BD}$, and sweat area under curve for 90 min ($AUC_{0-90,SBD}$), ranged ~15 min, 260 μM. min, and 133 μM. min, respectively. Since L-dopa may lower blood pressure, vital signs while seated were monitored throughout the visit (20, 38). The sitting mean arterial pressure (MAP) dropped (by 18 mm Hg) at the same timeline as BD_{max}, but recovered within 10 min of its

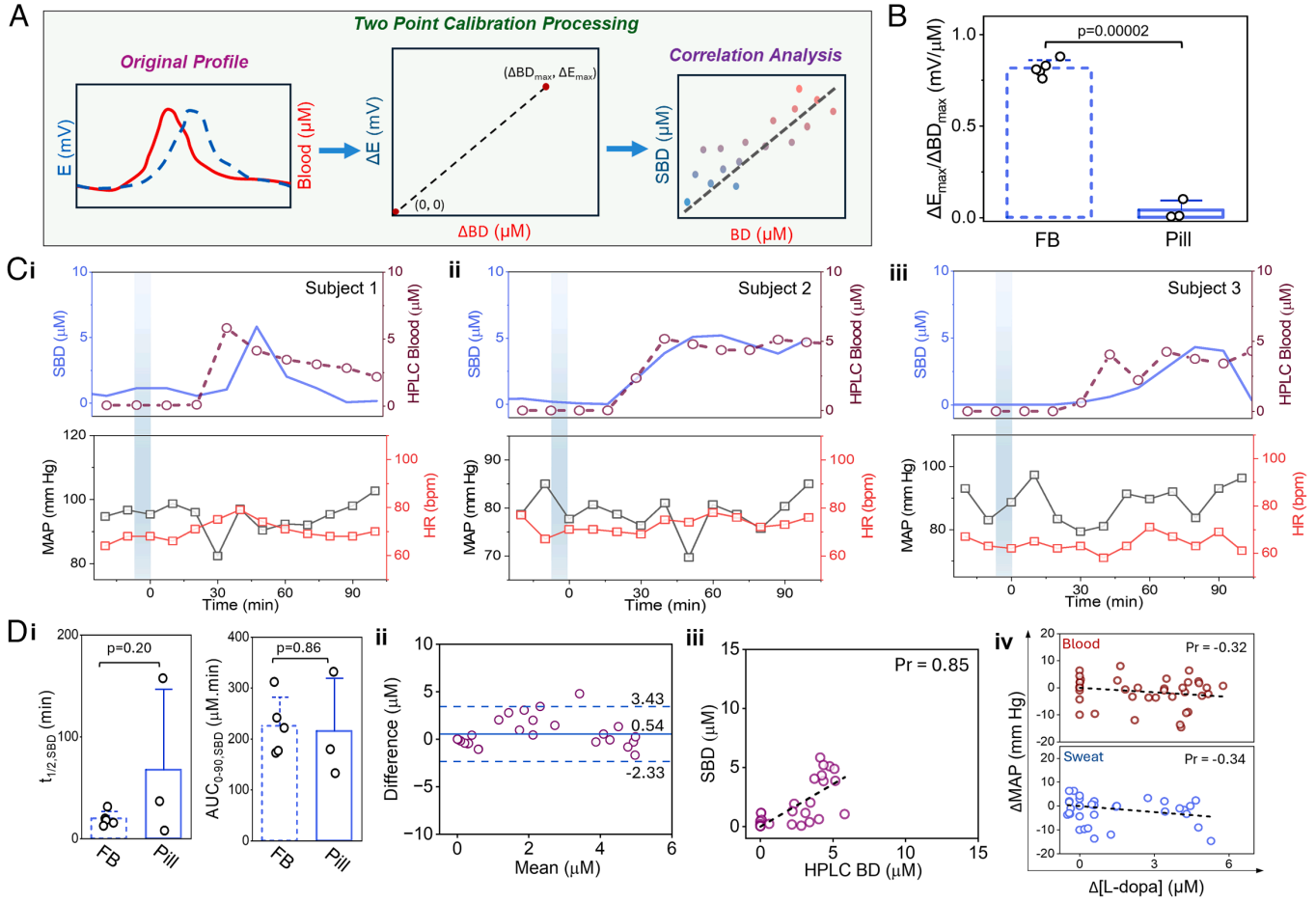

Fig. 4. S-CDM performance in healthy subjects under regular and clinical settings. (*A*) Schematic showing the two-point calibration method vs. blood L-dopa concentration (BD, capillary, and venous) for converting sensor potential reading to concentration values. The model assumes that when L-dopa in blood plasma is negligible, it corresponds to no change in the sensor potential reading. (*B*) Using this, personalized calibration parameters (calibration slope) are estimated for all subjects under varying conditions [fava bean (FB) and immediate-release L-dopa/carbidopa pill consumption]. FB resulted in a greater elevation in L-dopa compared to the oral levodopa-carbidopa tablet. Each data point represents a unique subject, n = 5 (FB), n = 3 (L-dopa/carbidopa pill). Significance is measured using the unpaired two sample *t* test. (*C*) (*i–iii*) *BD*(*t*) from HPLC, *SBD*(*t*) , MAP, and HR trends from all subjects. Blue vertical shaded area: L-dopa intake. (*D*) (*i*) Plot comparing $t_{1/2,SBD}$ and $AUC_{0-90,SBD}$ of FB vs. oral L-dopa. Statistical significance is measured using the unpaired two sample *t* test and error bars denote SD. (*ii*) Bland–Altman plot comparing the difference and mean of blood and sweat L-dopa concentrations following oral L-dopa/carbidopa intake. Dotted blue lines denote the limit of agreement (LOA; Mean ± 1.96 * SD). (*iii*) Correlation plot of blood vs. sweat L-dopa concentrations after oral L-dopa/carbidopa intake. The correlation coefficient was acquired through linear regression (n = 33 data points). (*iv*) Plot correlating MAP change vs. BD and SBD change after oral L-dopa/carbidopa intake. Negative correlation indicates L-dopa tends to induce acute hypotension. The correlation coefficient was acquired through linear regression (n = 33 data points).

peak minimum. The heart rate (HR) showed insignificant changes throughout the testing period (*SI Appendix*, Fig. S32). For subject 2 and 3, the clearance rate and $t_{1/2,BD}$ ranged ~0.0007 to 0.002 μM / min and ~300 to 1,000 min, respectively. Although all three subjects showed similar L-dopa absorption timelines in blood plasma with the same dosage, a low clearance rate and high $t_{1/2,BD}$ could arise due to individual factors such as lower quantities of L-dopa catalyzing enzymes in the blood and/or slower absorption at the intestine (4, 39, 40). $C_{max,BD}$ ranged ~4.5 to 5 μM (Fig. 4 *C, i–iii*), while $t_{max,BD}$ ranged ~30 to 60 min, post pill intake. $t_{lag,SBD}$ ranged ~15 to 20 min in both, $AUC_{0-90,BD}$ ranged ~335 μM. min and 246 μM. min, respectively, while $AUC_{0-90,SBD}$ ranged ~332 μM. min and 180 μM. min, respectively. Thus, similar AUC_{0-90} but different half-lives $t_{1/2,BD}$ suggest that even if subjects are exposed to the same drug dosage, the rate of L-dopa clearance from blood and its volume of distribution is subject-dependent. The MAP drop (by 8 mm Hg) occurred after 30 to 45 min in both subjects, while no significant changes were observed in the HR trends. Overall, the maximal MAP drop occurred around the same time as peak blood and sweat L-dopa in all three healthy subjects. Both blood and sweat Levodopa concentration profiles were fitted using a single-compartment model to evaluate the drug dynamics within their respective biofluids. No notable difference was found in $AUC_{0-90,SBD}$ between the pill and fava beans, likely due to the relatively fast L-dopa clearance from fava beans (Fig. 4 *D, i* and *SI Appendix*, Fig. S28). This also suggests that the net L-dopa bioavailability in sweat is comparable between fava beans and pill administration. Bland–Altman (BA) plot shows the mean difference between *BD*(*t*) and *SBD*(*t*) ranges ~0.54 μM and majority of the differences lie within −2.33 to 3.43 μM (Fig. 4 *D, ii*). The Pearson's correlation factor (*Pr*) between SBD and HPLC measured blood plasma ranged ~0.85 (Fig. 4 *D, iii*). *BD*(*t*) possessed a stronger (vs. *SBD*(*t*)) negative correlation ($Pr = -0.40$) with MAP primarily from proximal peak timelines and sustained effects from L-dopa (Fig. 4 *D, iv*). Overall, fava beans showed higher $\frac{\Delta E_{max}}{\Delta BD_{max}}$ (by 16 to 17 times vs. pill), but shorter $t_{lag,SBD}$, clearance rate, and $t_{1/2,BD}$, while maintaining a similar $AUC_{0-90,SBD}$, suggesting to serve as a rapid, short-term source of L-dopa in healthy individuals, while pills offer more sustained effects.

S-CDM Performance in Clinical PD Subjects with ML Analytics. S-CDM with our wireless FPCB was also tested on individuals with PD after taking a single dose of oral immediate-release L-dopa/carbidopa (*SI Appendix*, Fig. S33 and Table S5). The screening procedures are described in *SI Appendix*, *Supporting Information Text 7*. In summary, we measured L-dopa levels in sweat, collected venous blood for plasma HPLC analysis, and tracked blood pressure (BP) and heart rate trends. Clinicians assessed the motor score (MS) based on a modified Part III of the Movement Disorder Society-Sponsored Unified Parkinson's Disease Rating Scale (MDS-UPDRS) by serially observing changes in muscle rigidity, tremor, and bradykinesia/hypokinesia, where higher scores indicate more severe symptoms (Fig. 5*A* and *SI Appendix*, Table S6) (23). Fig. 5 *B, i–iv* shows the SBD and BD trends from four participants with PD.

All potentiometric responses are shown in *SI Appendix*, Fig. S34. $\Delta E(t)$ ranged ~1.5 to 2.5 mV, while average $\frac{\Delta E_{max}}{\Delta BD_{max}}$ ranged $\sim 0.19\ \mathrm{mV/\mu M}$ (*SI Appendix*, Fig. S34). $C_{max,BD}$ ranged ~7 to 18 μM, while $t_{max,BD}$ ranged ~80 min (subject 1 and 2) ~20 to 30 min (subject 3 and 4) after pill intake. BD trends also followed first-order kinetics with an average clearance rate of $\sim 0.017 \pm 0.002\ \mu\mathrm{M/min}$ and $t_{1/2,BD} \sim 39.36 \pm 5.84$ min, respectively (Fig. 4 *C, i–iii* and *SI Appendix*, Figs. S35 and S36). Calculated $SBD(t)$ showed average $t_{lag,SBD}$ of ~8 min, which is not only lower than healthy subjects, but also a common reported value for biological fluids (29, 41, 42). SBD also followed first-order kinetics with an average clearance rate of $\sim 0.037 \pm 0.022\ \mu\mathrm{M/min}$ and $t_{1/2,BD} \sim 25.18 \pm 14.83$ min, respectively, indicating L-dopa appears in sweat for a shorter duration compared to blood. With $SBD(t)$ increase, motor symptoms decreased, as expected. The lowest motor scores occurred within ~10 to 30 min of BD_{max} and SBD_{max} in all four subjects. The observed timeline corresponds well with existing literature, primarily capturing the period of L-dopa absorption in the gut (39, 43). Subjects 1 and showed elevated sitting MAP during/after taking the pill for a short duration (within 30 min), while Subject 2 and 3 showed declining and no change in sitting MAP trends, respectively, throughout the visit. Subject 4 also showed a MAP decrease within 30 min of pill intake, suggesting L-dopa's hypotensive effects.

The BA plot shows good alignment between the estimated $SBD(t)$ and $BD(t)$ from HPLC where the mean difference between them stands ~0.31 μM and majority of the differences lie within −6.75 to 6.12 μM (Fig. 5 *C, i*). The *Pr* ranged ~0.89 (Fig. 5 *C, ii*). The average $AUC_{0-90,BD}$ and $AUC_{0-90,SBD}$ measured $\sim 592 \pm 265\ \mu\mathrm{M.min}$ and $611 \pm 356\ \mu\mathrm{M.min}$, respectively, for PD but were not significantly different to the AUC metrics of healthy subjects (Fig. 5 *C, iii*). However, the blood plasma L-Dopa clearance rate was relatively faster (although statistically insignificant) for PD subjects in comparison to healthy subjects. Such trends can be attributed to several factors which are predominant in PD patients: fast dopaminergic metabolism, high AADC activity clearing L-dopa from blood (44), and faster L-dopa transport rate to the central nervous system (45, 46). Overall, these pharmacokinetic metrics indicates that both groups have similar L-dopa bioavailability in blood plasma and sweat, despite different elimination rates—a finding consistent with previous clinical studies and now assessed using our wearable device (45). Furthermore, despite the BP elevations in a few subjects, the overall negative *Pr* between MAP change and BD/SBD change confirmed L-dopa's tendency to predominantly induce hypotension, similar to its effect on healthy individuals (Fig. 5 *C, iv* and *SI Appendix*, Fig. S37).

We also conducted ML based analytics to evaluate which factors can contribute toward BD estimation (*SI Appendix*, *Supporting Information Text 8*). A support vector machine (SVM) based algorithm trained on SBD, BP, and MS values showed SBD to be the most influential feature for predicting BD, followed by diastolic blood pressure (DBP), MS, and systolic blood pressure (SBP) (Fig. 5 *D, i* and *SI Appendix*, Table S7). SBD remained also the dominant driver of BD prediction shifts, with higher sweat values (red trajectories) consistently driving the model output upward and lower values (blue trajectories) shifting it downward (Fig. 5 *D, ii*). DBP introduces additional variability, contributing moderate adjustments that either reinforce or partially offset the SBD trends. MS shows a smaller but noticeable incremental influence, fine-tuning predictions across individuals. In contrast, SBP exhibits comparatively limited deviation across most samples, with trajectories remaining relatively clustered near the cumulative trend established by preceding features. The predicted BD showed good agreement with HPLC-measured BD (coefficient of determination (R^2) = 0.85), with a mean difference of 0.31 μM (Fig. 5 *D, iii-iv*).

Discussion

Effective PD motor symptom management requires continuous and precise monitoring of L-dopa pharmacodynamic response to determine appropriate dosage. Current L-dopa quantification techniques (like HPLC and touch-based devices) deliver intermittent information and are impractical for providing real-time pharmacokinetic data in ambulatory settings due to several limitations: a) insufficiently accurate biofluid sampling methods; b) lack of power-efficient sensing strategies for sustained monitoring; and c) inability to capture personalized real-time pharmacodynamic profiles. Thus, patients rely on clinical consultation for their dosage adjustment decisions. Our S-CDM overcomes these limitations by offering a soft, conformal platform capable of tracking dynamic L-dopa profiles in real-time from the fingertip. It functions on an osmotic-driven passive sweat sampling strategy that operates under complete sedentary conditions with minimized sweat rate fluctuations, making it especially well-suited for people with PD in ambulatory settings. Efficient osmotic sweat withdrawal by the hydrogel is governed by the interplay between the hydrogen-bond network and crosslinking contributions with the osmolyte. Furthermore, it comprises a L-dopa sensor that runs on OCP (like a battery) with a potentiometric redox cycling scheme, making it independent from conventional voltametric scans. Through a personalized calibration approach, individualized calibration parameters were generated under varying physiological conditions to derive blood L-dopa pharmacodynamics on-the-go from sweat with greater accuracy, eventually reducing the need for frequent blood calibrations.

Initial testing on healthy subjects following fava bean consumption and after a single L-dopa/carbidopa oral tablet administration demonstrated the S-CDM's capability to successfully monitor temporal pharmacokinetic profiles. The measurements showed a lag time of 5 to 20 min and a *Pr* ~ 0.85, relative to plasma L-dopa concentrations measured by HPLC. Moreover, testing on four participants with PD yielded greater accuracy (higher *Pr* vs. blood plasma L-dopa), with lag time and *Pr* averaging around 5 to 6 min, and 0.89, respectively, further demonstrating the platform's potential for effective clinical use. These four PD participants exhibited a faster L-dopa clearance rate from blood compared to healthy subjects, but the net L-dopa bioavailability in blood and sweat remained similar. Blood pressure decreased for all healthy subjects under L-dopa administration. Acute hypotension and

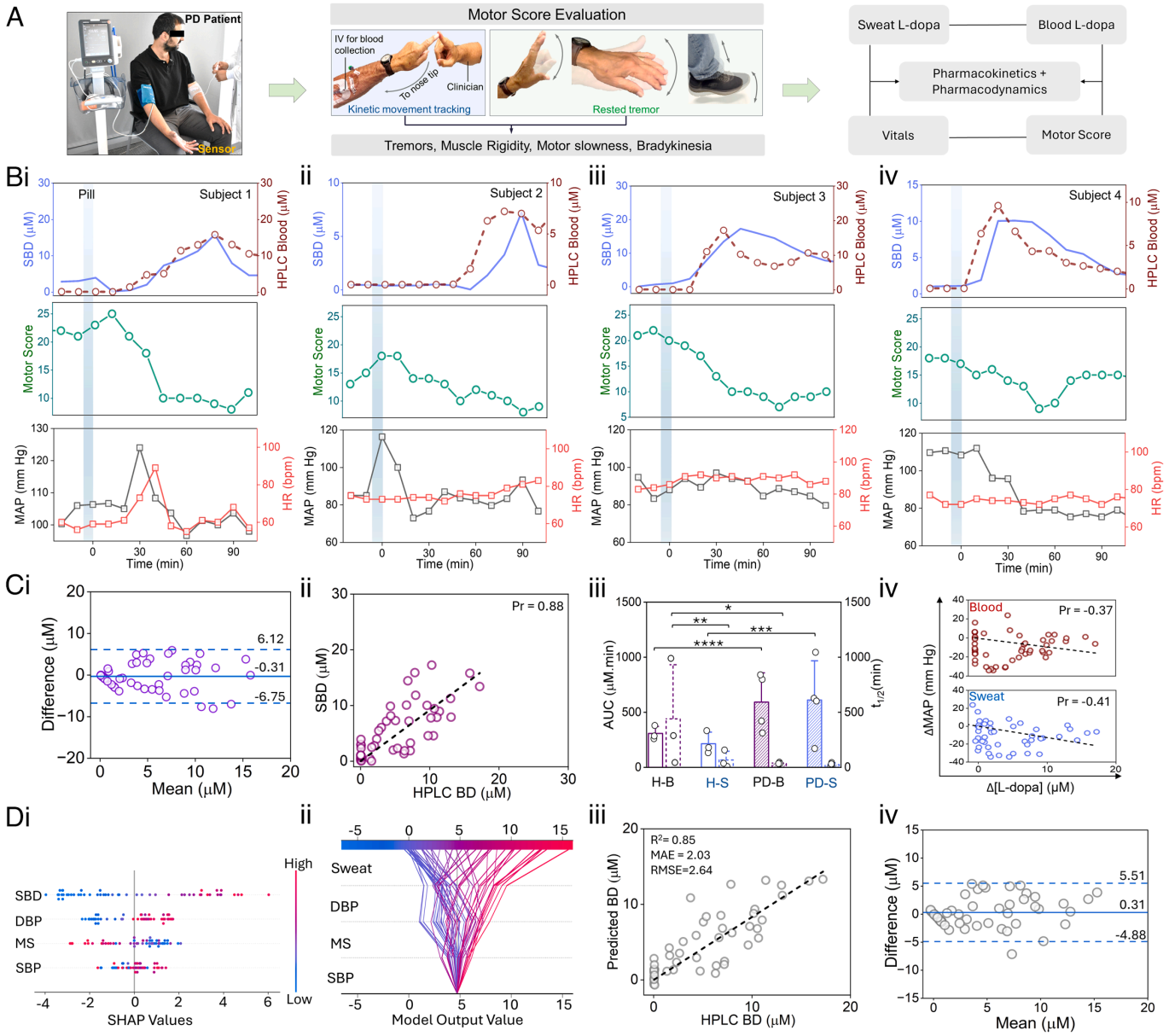

Fig. 5. S-CDM performance in participants with PD. (*A*) Image of a participant with PD with the S-CDM on the fingertip. We serially measured L-dopa in sweat and plasma (with HPLC), motor score severity, blood pressure, and heart rate from participants at 10-min intervals. The motor score was evaluated by a movement disorders neurologist using a modified Movement Disorders Society Unified Parkinson's Disease Rating Scale (MDS-UPDRS) Part III, rating items for bradykinesia, rigidity, and tremor, where higher scores indicate more severe motor symptoms. (*B*) (*i–iv*) Plots showing the SBD, BD, motor score, MAP, and HR from four participants with PD after immediate-release oral L-dopa/carbidopa intake. $\frac{\Delta E_{max}}{\Delta BD_{max}} = 0.19$ was used to convert potential to concentration values for all subjects. (*C*) (*i*) Bland–Altman plot comparing the difference and the mean of L-dopa concentrations from plasma (via HPLC) and sweat. Dotted blue lines denote LOA. (*ii*) Correlation plot of plasma vs. sweat L-dopa concentrations. The correlation coefficient was acquired through linear regression (n = 40 data points). (*iii*) Plot comparing AUC_{0-90} (solid edge) and $t_{1/2}$ (dashed edge) of healthy vs. PD patients from plasma and sweat after a single dosage of oral immediate-release L-dopa/carbidopa. H-B: Healthy blood, H-S: Healthy sweat, PD-B: Parkinson's blood and PD-S: Parkinson's sweat. Each dot represents a unique subject. Significance is measured using the unpaired two sample *t* test and error bars denote SD. *P = 0.15, **P = 0.29, ***P = 0.12, ****P = 0.13. (*iv*) Plot correlating MAP change vs. BD and SBD change shows a negative correlation, indicating L-dopa concentrations are associated with acute hypotension. The correlation coefficient was acquired through linear regression (n = 52 points). (*D*) (*i* and *ii*) SHAP summary and decision plots from the SVM algorithm highlighting the relative contributions of sweat, blood pressure, and motor score toward BD estimation. (*iii* and *iv*) Correlation and Bland–Altman plots showing the agreement between the predicted and HPLC measured BD (n = 55 data points). MAE: Mean absolute error, RMSE: Root mean square error. Dotted gray lines denote LOA.

worsening orthostatic hypotension (OH) from L-dopa intake are widely reported in individuals with PD, but we observed similar trends in healthy subjects as well (20, 21, 47, 48). The PD motor symptoms showed an inverse correlation with BD and SBD, supporting the expected improvement in motor symptoms corresponding with L-dopa pharmacodynamics. In PD participants, BP changes showed mixed trends after levodopa administration, with predominant hypotensive trends (20, 49–51). Finally, ML analysis identified sweat and DBP as the primary contributors for dictating BD variations, and their integration enabled accurate prediction of BD compared to HPLC-derived values. Overall, as wearable L-dopa monitoring in epidermal biofluids is still an emerging field without established clinical benchmarks, our clinical metrics demonstrate a promising step toward this goal.

To realize the full potential of our S-CDM in clinical and at-home PD management, future work will prioritize large-scale clinical validation across diverse PD patient populations to further validate the robustness of the system across varying PD

stages, medication regimens, and physiological conditions. Improved understanding of how L-Dopa levels correlate with motor performance will allow clinicians to define the target therapeutic range(s) for L-dopa and to treat PD symptoms with the minimal effective L-dopa dose to prevent motor complications. Expanding the platform to track responses from multiple L-dopa doses throughout the day will also be essential for capturing dynamic intraindividual fluctuations and to guide real-time therapeutic decisions. Applying a two-compartment pharmacokinetic (PK) model to fit both sweat and blood concentration profiles would further improve understanding of the partitioning mechanism of L-dopa from blood into sweat. Furthermore, merging physiological sensors (such as for vital signs) with L-dopa sensors into a single form factor will further enable a more comprehensive understanding of drug response and motor symptom dynamics. AI-driven models trained with large datasets will even allow the system to continuously refine individualized calibration parameters, concentration outputs, and blood-sweat time lag, enhancing both accuracy and adaptability over time. It would also help make the results less dependent on specific datasets, thereby improving the model's generalizability across patients. Finally, as L-dopa concentrations inform personalized L-dopa regimen adjustments in PD, there is a strong potential for integration with continuous L-dopa infusion technologies into closed-loop systems. Given the key requirements of an ideal closed-loop system—prevalidation of sensing and delivery components in large, extensive clinical trials, high accuracy and reliability, fast response time, hassle-free operation, power efficient operation to sustain longevity, and have proper clinical validation (52)—we believe our S-CDM system holds considerable promise to serve as a valuable component for future autonomous and power efficient wearable closed-loop platforms.

Data, Materials, and Software Availability. All study data are included in the article and/or supporting information.

ACKNOWLEDGMENTS. This research was supported by the University of California, San Diego (UCSD) Center of Wearable Sensors, NIH 1R01NS141451-01, and Emory HPLC Bioanalytical Core (RRID:SCR_023531). We would like to thank UCSD's Nano3 cleanroom and Design and Innovation Center for their assistance with fabrication and instrumentation facility. We acknowledge the use of facilities and instrumentation supported by the NSF through the University of California San Diego Materials Research Science and Engineering Center (UC San Diego MRSEC) DMR-2011924. We would like to thank Dr. Rachel Blau for assistance with hydrogel Fourier-Transform Infrared (FTIR) spectroscopy. D.D. acknowledges Prof. Jonathan K. Pokorski for support through the UC San Diego MRSEC program. B.S acknowledges support from the Fullbright Israel Fellowship Program. A.A. acknowledges financial support from the Kuwait Foundation for the Advancement of Sciences. A.J. was supported by the Polish National Agency for Academic Exchange under the Bekker program (Grant No. BPN/BEK/2023/1/00139/U/00001).

Author affiliations: [a]Aiiso Yufeng Li Family Department of Chemical and Nanoengineering, University of California, San Diego, La Jolla, CA 92093; [b]Department of Neurosciences, University of California, San Diego, La Jolla, CA 92093; [c]Department of Electrical and Computer Engineering, University of California, San Diego, La Jolla, CA 92161; and [d]Department of Mechanical Engineering, University of California, San Diego, La Jolla, CA 92161

Author contributions: T.S., K.L., M.S., E.S., and J.W. designed research; T.S., M.I.K., K.L., B.S., K.Z., H.d.M., G.J., B.C., Z.W., R.P., E.S., D.D., A.J., S.D., and L.Y. performed research; T.S., R.P., M.R., C.M., A.A., S.S.S., P.N., and J.W. contributed new reagents/analytic tools; T.S., M.I.K., K.L., I.L., and J.W. analyzed data; I.L. funding acquisition and co-corresponding authorship with J.W.; and T.S. wrote the paper.

The authors declare no competing interest.

1. C. Marras *et al.*, Prevalence of Parkinson's disease across North America. *npj Parkinson's Dis.* **4**, 1–7 (2018).
2. E. R. Dorsey, T. Sherer, M. S. Okun, B. R. Bloemd, The emerging evidence of the Parkinson pandemic. *J. Parkinson's Dis.* **8**, S3–S8 (2018).
3. W. Yang *et al.*, Current and projected future economic burden of Parkinson's disease in the U.S. *npj Parkinson's Dis.* **6**, 15 (2020).
4. D. Probst, K. Batchu, J. R. Younce, K. Sode, Levodopa: From biological significance to continuous monitoring. *ACS Sens.* **9**, 3828–3839 (2024).
5. G. M. Maddocks, M. Eisenstein, H. T. Soh, Biosensors for Parkinson's disease: Where are we now, and where do we need to go? *ACS Sensors* **9**, 4307–4327 (2024).
6. W. Poewe *et al.*, Parkinson disease. *Nat. Rev. Dis. Prim.* **3**, 17013 (2017).
7. M. H. G. Monje, G. Foffani, J. Obeso, Á. Sánchez-Ferro, New sensor and wearable technologies to aid in the diagnosis and treatment monitoring of Parkinson's disease. *Annu. Rev. Biomed. Eng.* **21**, 111–143 (2019).
8. C. Livingston, L. Monroe-Duprey, A review of levodopa formulations for the treatment of Parkinson's disease available in the United States. *J. Pharm. Pract.* **37**, 485–494 (2024).
9. N. Tambasco, M. Romoli, P. Calabresi, Levodopa in Parkinson's disease: Current status and future developments. *Curr. Neuropharmacol.* **16**, 1239–1252 (2018).
10. D. Urso, K. R. Chaudhuri, M. A. Qamar, P. Jenner, Improving the delivery of levodopa in Parkinson's disease: A review of approved and emerging therapies. *CNS Drugs* **34**, 1149–1163 (2020).
11. H. Teymourian *et al.*, Closing the loop for patients with Parkinson disease: Where are we? *Nat. Rev. Neurol.* **18**, 497–507 (2022).
12. C. W. Olanow, L. L. Gauger, J. M. Cedarbaum, Temporal relationships between plasma and cerebrospinal fluid pharmacokinetics of levodopa and clinical effect in Parkinson's disease. *Ann. Neurol.* **29**, 556–559 (1991).
13. V. Leta *et al.*, Gastrointestinal barriers to levodopa transport and absorption in Parkinson's disease. *Eur. J. Neurol.* **30**, 1465–1480 (2023).
14. J. Moon *et al.*, Non-invasive sweat-based tracking of L-Dopa pharmacokinetic profiles following an oral tablet administration. *Angew. Chem. Int. Ed.* **60**, 19074–19078 (2021).
15. Y. Zhou *et al.*, A nanoMIP sensor for real-time in vivo monitoring of levodopa pharmacokinetics in precision Parkinson's therapy. *Nat. Commun.* **16**, 10796 (2025).
16. K. Mahato *et al.*, Biosensor strip for rapid on-site assessment of levodopa pharmacokinetics along with motor performance in Parkinson's disease. *Angew. Chemie Int. Ed.* **63**, e202403583 (2024).
17. L. Rigon, C. Fogliano, P. Odin, A. Antonini, Infusion therapies for Parkinson's disease: Where are we in 2025? *Expert Opin. Drug Deliv.* **23**, 187–190 (2025).
18. N. A. S. Taylor, C. A. Machado-Moreira, Regional variations in transepidermal water loss, eccrine sweat gland density, sweat secretion rates and electrolyte composition in resting and exercising humans. *Extrem. Physiol. Med.* **2**, 4 (2013).
19. T. Saha *et al.*, A passive perspiration inspired wearable platform for continuous glucose monitoring. *Adv. Sci.* **11**, 1–15 (2024).
20. T. Earl *et al.*, Effect of levodopa on postural blood pressure changes in Parkinson disease: A randomized crossover study. *Clin. Auton. Res.* **34**, 117–124 (2024).
21. J. K. Cutsforth-Gregory, P. A. Low, Neurogenic orthostatic hypotension in Parkinson disease: A primer. *Neurol. Ther.* **8**, 307–324 (2019).
22. MDS-Unified Parkinson's disease rating scale (MDS-UPDRS). https://www.movementdisorders.org/MDS/MDS-Rating-Scales/MDS-Unified-Parkinsons-Disease-Rating-Scale-MDS-UPDRS.htm. Accessed 1 May 2026.
23. C. G. Goetz *et al.*, Movement disorder society-sponsored revision of the Unified Parkinson's Disease Rating Scale (MDS-UPDRS): Scale presentation and clinimetric testing results. *Mov. Disord.* **23**, 2129–2170 (2008).
24. T. Saha *et al.*, Wireless wearable electrochemical sensing platform with zero-power osmotic sweat extraction for continuous lactate monitoring. *ACS Sens.* **7**, 2037–2048 (2022).
25. T. Saha, J. Fang, S. Mukherjee, M. D. Dickey, O. D. Velev, Wearable osmotic-capillary patch for prolonged sweat harvesting and sensing. *ACS Appl. Mater. Interfaces* **13**, 8071–8081 (2021).
26. K. Y. Goud *et al.*, Wearable electrochemical microneedle sensor for continuous monitoring of levodopa: Toward Parkinson management. *ACS Sens.* **4**, 2196–2204 (2019).
27. L. C. Tai *et al.*, Wearable sweat band for noninvasive levodopa monitoring. *Nano Lett.* **19**, 6346–6351 (2019).
28. H. Y. Y. Nyein *et al.*, A wearable patch for continuous analysis of thermoregulatory sweat at rest. *Nat. Commun.* **12**, 1823 (2021).
29. J. Min *et al.*, Skin-interfaced wearable sweat sensors for precision medicine. *Chem. Rev.* **123**, 5049–5138 (2023).
30. L. Yin *et al.*, A stretchable epidermal sweat sensing platform with an integrated printed battery and electrochromic display. *Nat. Electron.* **5**, 694–705 (2022).
31. A. J. Bandodkar *et al.*, Battery-free, skin-interfaced microfluidic/electronic systems for simultaneous electrochemical, colorimetric, and volumetric analysis of sweat. *Sci. Adv.* **5**, eaav3294 (2019).
32. R. Randhir, D. Vattem, K. Shetty, Solid-state bioconversion of fava bean by *Rhizopus oligosporus* for enrichment of phenolic antioxidants and L-DOPA. *Innov. Food Sci. Emerg. Technol.* **5**, 235–244 (2004).
33. M. Rijntjes, Knowing your beans in Parkinson's disease: A critical assessment of current knowledge about different beans and their compounds in the treatment of Parkinson's disease and in animal models. *Parkinson's Dis.* **2019**, 1349509 (2019).
34. O. Djassemi *et al.*, A touch enabled hemodynamic and metabolic monitor. *Adv. Sci.* **12**, e2502138 (2025).
35. J. R. Sempionatto, J.-M. Moon, J. Wang, Touch-based fingertip blood-free reliable glucose monitoring: Personalized data processing for predicting blood glucose concentrations. *ACS Sens.* **6**, 1875–1883 (2021).
36. M. Contin, P. Martinelli, Pharmacokinetics of levodopa. *J. Neurol.* **257**, S253–S261 (2010).
37. D. Nyholm *et al.*, Pharmacokinetics of levodopa, carbidopa, and 3-O-methyldopa following 16-hour jejunal infusion of levodopa-carbidopa intestinal gel in advanced Parkinson's disease patients. *AAPS J.* **15**, 316–323 (2013).
38. R. P. Irwin, J. G. Nutt, W. R. Woodward, S. T. Gancher, Pharmacodynamics of the hypotensive effect of levodopa in Parkinsonian patients. *Clin. Neuropharmacol.* **15**, 365–374 (1992).
39. C. Rusch, R. Flanagan, H. Suh, I. Subramanian, To restrict or not to restrict? Practical considerations for optimizing dietary protein interactions on levodopa absorption in Parkinson's disease. *npj Parkinson's Dis.* **9**, 1–8 (2023).
40. M. Beckers, B. R. Bloem, M. M. Verbeek, Mechanisms of peripheral levodopa resistance in Parkinson's disease. *npj Parkinson's Dis.* **8**, 56 (2022).

41. T. Saha *et al.*, Wearable electrochemical glucose sensors in diabetes management: A comprehensive review. *Chem. Rev.* **123**, 7854–7889 (2023).
42. M. Friedel *et al.*, Opportunities and challenges in the diagnostic utility of dermal interstitial fluid. *Nat. Biomed. Eng.* **7**, 1541–1555 (2023).
43. A. Demailly, C. Moreau, D. Devos, Effectiveness of continuous dopaminergic therapies in Parkinson's disease: A review of L-DOPA pharmacokinetics/pharmacodynamics. *J. Parkinson's Dis.* **14**, 925–939 (2024).
44. A. van Rumund *et al.*, Peripheral decarboxylase inhibitors paradoxically induce aromatic L-amino acid decarboxylase. *npj Parkinson's Dis.* **7**, 29 (2021).
45. H. Iwaki *et al.*, Pharmacokinetics of levodopa/benserazide versus levodopa/carbidopa in healthy subjects and patients with Parkinson's disease. *Neurol. Clin. Neurosci.* **3**, 68–73 (2015).
46. M. Kuoppamäki *et al.*, Comparison of pharmacokinetic profile of levodopa throughout the day between levodopa/carbidopa/entacapone and levodopa/carbidopa when administered four or five times daily. *Eur. J. Clin. Pharmacol.* **65**, 443–455 (2009).
47. T. L. Whitsett, L. I. Goldberg, Effects of levodopa on systolic preejection period, blood pressure, and heart rate during acute and chronic treatment of Parkinson's disease. *Circulation* **45**, 97–106 (1972).
48. A. Fanciulli, F. Leys, C. Falup-Pecurariu, R. Thijs, G. K. Wenning, Management of orthostatic hypotension in Parkinson's disease. *J. Parkinson's Dis.* **10**, S57–S64 (2020).
49. C. C. Huang *et al.*, Effectiveness of different methods for baroreflex sensitivity assessment in determining the severity of cardiovascular autonomic neuropathy in patients with Parkinson's disease. *Front. Neurosci.* **16**, 1–8 (2022).
50. J. L. Sabino-Carvalho, B. Falquetto, A. C. Takakura, L. C. Vianna, Baroreflex dysfunction in Parkinson's disease: Integration of central and peripheral mechanisms. *J. Neurophysiol.* **125**, 1425–1439 (2021).
51. R. F. Pfeiffer, Autonomic dysfunction in Parkinson's disease. *Neurotherapeutics* **17**, 1464–1479 (2020).
52. M. M. Paci *et al.*, Smart closed-loop drug delivery systems. *Nat. Rev. Bioeng.* **3**, 816–834 (2025).